ATLAS NOTE

ATLAS-CONF-2017-020

22nd March 2017

Search for a Scalar Partner of the Top Quark in the Jets+E_T^{miss} Final State at $\sqrt{s}=13$ TeV with the ATLAS detector

The ATLAS Collaboration

Abstract

A search for direct pair production of a scalar partner to the top quark in events with four or more jets plus missing transverse momentum is presented. An analysis of 36 fb^{-1} of $\sqrt{s}=13$ TeV proton–proton collisions collected using the ATLAS detector at the LHC yielded no significant excess over the Standard Model background expectation. To interpret the results a supersymmetric model is used where the top squark is assumed to decay via $\tilde{t} \to t^{(*)}\tilde{\chi}_1^0$, where $\tilde{\chi}_1^0$ denotes the lightest neutralino. Exclusion limits are placed in terms of the top squark and neutralino masses. Assuming branching fractions of 100% to $t\tilde{\chi}_1^0$, top squark masses in the range 450−950 GeV are excluded for $\tilde{\chi}_1^0$ masses below 160 GeV. In the case where $m_{\tilde{t}} \sim m_t + m_{\tilde{\chi}^0}$ top squark masses between 235−590 GeV are excluded.

1 Introduction

Supersymmetry (SUSY) [1–6] is an extension of the Standard Model (SM) that can resolve for example the gauge hierarchy problem [7–10] by introducing supersymmetric partners of the known bosons and fermions. The SUSY partner to the top quark, the top squark[1] ($\tilde{t}$), plays an important role in canceling potentially large top-quark loop corrections in the Higgs-boson mass.

In R-parity conserving SUSY models [11], the supersymmetric partners are produced in pairs. Top squarks are produced by strong interactions through quark-antiquark ($q\bar{q}$) annihilation or gluon-gluon fusion, and the production cross section of direct top squark pairs is largely decoupled from the specific choice of SUSY model parameters [12–15]. The decay of the top squark depends on the masses, the mixing of the superpartners of left- and right-handed top quarks, and the mixing parameters of the fermionic partners of the electroweak and Higgs bosons, which are collectively known as charginos, $\tilde{\chi}_i^\pm$, $i = 1, 2$, and neutralinos, $\tilde{\chi}_i^0$, $i = 1, ..., 4$, where $\tilde{\chi}_1^0$ is the lightest supersymmetric particle (LSP) and $\tilde{\chi}_2^0$ is the next lightest supersymmetric particle (NLSP). Two different decay scenarios are considered in this search: (a) both top squarks decay via $\tilde{t} \to t^{(*)} \tilde{\chi}_1^0$ and (b) at least one of the top squarks decay via $\tilde{t} \to b\tilde{\chi}_1^\pm \to bW^{(*)}\tilde{\chi}_1^0$, with various hypotheses for $m_{\tilde{\chi}^0}$ and $m_{\tilde{\chi}_1^\pm}$, as illustrated in Fig. 1(a)−(b), respectively. The lightest neutralino, $\tilde{\chi}_1^0$, is stable and a dark matter candidate [16, 17]. Interpretations for scenario (a) are provided in this note using simplified models where only one decay step is allowed. A grid of signal samples are generated across the plane of the top squark and $\tilde{\chi}_1^0$ masses with a grid spacing of 50 GeV across most of the plane assuming the chirality of the top squark resulting from maximal mixing between left and right-handed top squarks.

In addition to direct pair production, top squarks can be produced indirectly through gluino decays, as shown in Fig. 1(c). This search considers models where the mass difference between the top squark and the neutralino is small, i.e., $\Delta m(\tilde{t}, \tilde{\chi}_1^0) = 5$ GeV. In this scenario, the jets originating from the $\tilde{t}$ decays have low momenta compared to experimental acceptance resulting in a nearly identical signature to $\tilde{t} \to t\tilde{\chi}_1^0$ signal models.

(a) $\tilde{t} \to t^{(*)} \tilde{\chi}_1^0$ (b) $\tilde{t} \to b\tilde{\chi}_1^\pm \to bW^{(*)}\tilde{\chi}_1^0$ (c) $\tilde{g} \to t\tilde{t} \to t\tilde{\chi}_1^0$+soft
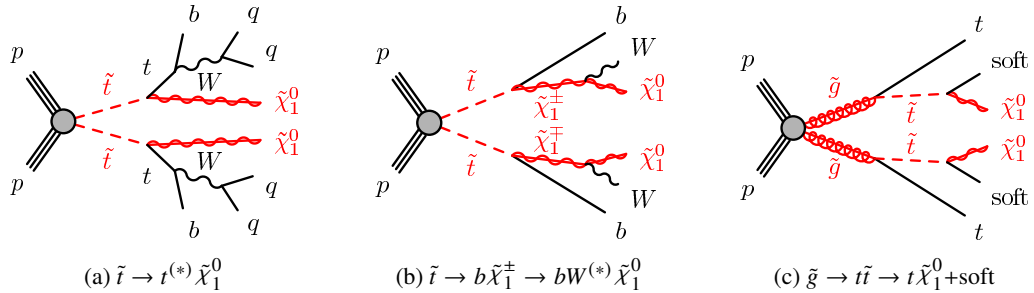
Figure 1: The decay topologies of the signal models considered with experimental signatures of four or more jets plus missing transverse momentum.

This note presents a search for top-squark pair production using a time-integrated luminosity of $\int \mathcal{L}\, dt = (36.1 \pm 1.2)$ fb^{-1} of pp collisions data provided by the Large Hadron Collider (LHC) at a center-of-mass

---

[1] The superpartners of the left- and right- handed top quarks, $\tilde{t}_L$ and $\tilde{t}_R$, mix to form the two mass eigenstates $\tilde{t}_1$ and $\tilde{t}_2$, where $\tilde{t}_1$ is the lighter one. Throughout this note $\tilde{t}_1$ is noted as $\tilde{t}$.

energy of $\sqrt{s} = 13$ TeV. The data were collected by the ATLAS detector in 2015 and 2016. All-hadronic final states with at least four jets and large missing transverse momentum ($\mathbf{p}_{\mathrm{T}}^{\mathrm{miss}}$, whose magnitude is referred to as $E_{\mathrm{T}}^{\mathrm{miss}}$) are considered, and the results are interpreted according to a variety of signal models as described above. Signal regions are defined to maximize the experimental sensitivity over a large range of kinematic phase space. Sensitivity to high top-squark masses ~ 1000 GeV (as in Fig. 1(a)) and top squarks produced through gluino decays (as in Fig. 1(c)) are achieved by exploiting techniques designed to reconstruct top quarks that are Lorentz-boosted in the lab frame. The dominant SM background process for this kinematic region is $Z \rightarrow \nu\bar{\nu}$ produced in association with jets initiated by heavy-flavor quarks. Sensitivity to the region where $m_{\tilde{t}} - m_{\tilde{\chi}_1^0} \sim m_t$, which typically has relatively low-p_{T} final state objects and low $E_{\mathrm{T}}^{\mathrm{miss}}$, is achieved by exploiting events in which high-p_{T} jets from initial-state radiation (ISR) boosts the di-top-squark system in the transverse plane. For this regime, $t\bar{t}$ production makes up the dominant background contribution. Similar searches based on $\sqrt{s} = 8$ TeV and $\sqrt{s} = 13$ TeV data collected at the LHC have been performed by both the ATLAS [18, 19] and CMS [20–24] collaborations.

2 ATLAS detector

The ATLAS experiment [25] at the LHC is a multi-purpose particle detector with a cylindrical forward-backward symmetric geometry[2] and an approximate 4π coverage in solid angle. It consists of an inner tracking detector surrounded by a thin superconducting solenoid providing a 2 T axial magnetic field, electromagnetic and hadron calorimeters, and a muon spectrometer. The inner tracking detector covers the pseudorapidity range $|\eta| < 2.5$. It consists of silicon pixel, silicon micro-strip, and transition radiation tracking detectors. The newly installed innermost layer of pixel sensors [26] was operational for the first time during the 2015 data taking. Lead/liquid-argon (LAr) sampling calorimeters provide electromagnetic (EM) energy measurements with high granularity. A hadron (steel/scintillator-tile) calorimeter covers the central pseudorapidity range ($|\eta| < 1.7$). The end-cap and forward regions are instrumented with LAr calorimeters for both EM and hadronic energy measurements up to $|\eta| = 4.9$. The muon spectrometer surrounds the calorimeters and is based on three large air-core toroid superconducting magnets with eight coils each. The average toroid field strength is approximately 0.5 T in the central region and 1 T in the end-cap regions. It includes a system of precision tracking chambers and fast detectors for triggering.

3 Trigger and data collection

The data were collected from August to November 2015 and April to October 2016 at a pp centre-of-mass energy of 13 TeV with 25 ns bunch spacing. A two-level trigger system [27] is used to select events. The first-level trigger is implemented in hardware and uses a subset of the detector information to reduce the accepted rate to at most 100 kHz. This is followed by a software-based trigger that reduces the accepted event rate to 1 kHz for offline storage.

---

[2] ATLAS uses a right-handed coordinate system with its origin at the nominal interaction point (IP) in the centre of the detector and the z-axis along the beam pipe. The x-axis points from the IP to the centre of the LHC ring, and the y-axis points upwards. Cylindrical coordinates (r, ϕ) are used in the transverse plane, ϕ being the azimuthal angle around the z-axis. The pseudorapidity is defined in terms of the polar angle θ as $\eta = -\ln\tan(\theta/2)$. Angular distance is measured in units of $\Delta R \equiv \sqrt{(\Delta\eta)^2 + (\Delta\phi)^2}$.

In all search regions, a missing transverse momentum trigger, which is fully efficient for offline calibrated $E_T^{miss} > 250$ GeV in signal events, was used to collect data events. The luminosity uncertainty of 2.1% (3.4%) for data taken in 2015 (2016) is derived following the same methodology as that detailed in Refs. [28], from a preliminary calibration of the luminosity scale obtained from beam-separation scans performed in August 2015 (May 2016).

Data samples enriched in the major sources of background were collected with electron or muon triggers. The electron trigger selects events based on the presence of clusters of energy in the electromagnetic calorimeter, with a shower shape consistent with that expected for an electron, and a matching track in the tracking system. The muon trigger selects events containing one or more muon candidates based on tracks identified in the muon spectrometer and inner detector. The electron and muon triggers used are > 99% efficient for isolated electrons and muons with p_T of 28 GeV and above.

Triggers based on the presence of high-p_T jets are used to collect data samples for the estimation of the multijet and all-hadronic $t\bar{t}$ background. The jet p_T thresholds ranged from 20 to 400 GeV. In order to stay within the bandwidth limits of the trigger system, only a fraction of events passing these triggers were recorded to permanent storage.

4 Simulated event samples and signal modelling

Simulated events are used to model the SUSY signal and to aid in the description of the background processes. Signal models are all generated with MG5_aMC@NLO [29] interfaced to PYTHIA8 [30] for the parton showering (PS) and hadronisation and with EvtGen v1.2.0 program [31] as an afterburner for b-hadron decays. The matrix element (ME) calculation is performed at tree-level and includes the emission of up to two additional partons for all signal samples. The parton distribution function (PDF) set used for the generation of the signal samples is NNPDF2.3LO [32] with A14 set [33] for the underlying-event and shower parameters (UE tune). The ME-PS matching is performed with the CKKW-L [34] prescription, with a matching scale set to one quarter of the mass of the $\tilde{t}$, or $\tilde{g}$ for the gluino pair production model. Signal cross sections are calculated to next-to-leading order in the strong coupling constant, adding the resummation of soft-gluon emission at next-to-leading-logarithmic accuracy (NLO+NLL) [12–14]. The nominal cross section and the uncertainty are taken from an envelope of cross-section predictions using different PDF sets and factorization and renormalization scales, as described in Ref. [15].

SM background samples are generated with different MC generators depending on the process. The background sources of Z + jets and W + jets events are generated with SHERPAv2.2.1 [35] using the NNPDF3.0NNLO [32] PDF set and the UE tune provided by SHERPA. Top-quark pair production where at least one of the top quarks decays to a lepton and single-top production are simulated with Powheg-Boxv.2 [36] and interfaced to PYTHIA6 [37] for PS and hadronisation, with the CT10 [38] PDF set and using the Perugia2012 [39] set of tuned parameters. MG5_aMC@NLO interfaced to PYTHIA8 for PS and hadronisation is used to generate the $t\bar{t}$+V (where V is W or Z) and $t\bar{t}+\gamma$ samples at NLO with the NNPDF3.0NLO PDF set. The underlying-event tune used is A14 with the NNPDF2.3LO PDF set. Diboson production is generated with SHERPAv2.2.1 using the CT10 PDF set. Finally, $V\gamma$ processes are generated with SHERPAv2.1 using the CT10 PDF set. Additional information can be found in Refs. [40–44].

The detector simulation [45] is performed using either GEANT4 [46] or a fast simulation framework where the showers in the electromagnetic and hadronic calorimeters are simulated with a parameterized

description [47] and the rest of the detector is simulated with GEANT4. The fast simulation was validated against full GEANT4 simulation for several selected signal samples and subsequently used for all signal samples due to the large number of signal grid points needed for various interpretations. All standard model background samples used the GEANT4 setup. All MC samples are produced with a varying number of simulated minimum-bias interactions overlaid on the hard-scattering event to account for multiple pp interactions in the same or nearby bunch crossing (pileup). These events are produced using PYTHIA8 with the A2 tune [48] and MSTW 2008 PDF set [49]. The simulated events are reweighted to match the distribution of number of interaction in data. Corrections are applied to the simulated events to correct for differences between data and simulation for the lepton-trigger and reconstruction efficiencies, momentum scale, energy resolution, isolation, and for the efficiency of identifying jets containing b-hadrons, together with the probability for mis-tagging jets containing light-flavor and charm hadrons.

5 Event and physics object reconstruction

Events are required to have a primary vertex [50] reconstructed from at least two associated tracks with $p_T > 400$ MeV. Among the vertices found, the vertex with the largest summed p_T^2 of the associated tracks is chosen.

Jets are reconstructed from three-dimensional topological clusters of noise-suppressed calorimeter cells [51] using the anti-k_t jet algorithm [52, 53] with a distance parameter $R = 0.4$. An area-based correction is applied to account for energy from additional pp collisions based on an estimate of the pileup activity in a given event [54]. Calibrated [55] jet candidates are required to have $p_T > 20$ GeV and $|\eta| < 2.8$. Events containing jets arising from non-collision sources or detector noise [56] are removed. Additional selections are applied to jets with $p_T < 60$ GeV and $|\eta| < 2.4$ to reject events that originate from pileup interactions [57].

Jets containing b-hadrons ("b-jets") and which are within the inner detector acceptance ($|\eta| < 2.5$) are identified (b-tagged) with a multivariate algorithm that exploits the impact parameters of the charged-particle tracks, the presence of secondary vertices and the reconstructed flight paths of b- and c-hadrons inside the jet [58–60]. The output of the multivariate algorithm is a single b-tagging weight which signifies the likelihood of a jet containing b-hadrons. The average identification efficiency of jets containing b-hadrons is 77% as measured with simulated $t\bar{t}$ events. A rejection factor of approximately 134 is reached for light-quark and gluon jets and 6.2 for charm jets (depending on the p_T of the jet).

Electron candidates are reconstructed from energy clusters in the electromagnetic calorimeter that are matched to a track in the inner detector. They are required to have $|\eta| < 2.47$, $p_T > 7$ GeV and must pass a variant of the "very loose" likelihood-based selection [61]. The electromagnetic shower of an electron can also form a jet such that a procedure is required to resolve this ambiguity. In the case where the separation between an electron candidate and a non-b-tagged (b-tagged) jet is $\Delta R < 0.2$[3], the object is considered to be an electron (b-tagged jet). If the separation between an electron candidate and any jet satisfies $0.2 < \Delta R < 0.4$, the object is considered to be a jet, and the electron candidate is removed. Muons are reconstructed from matching tracks in the inner detector and in the muon spectrometer and are required to have $|\eta| < 2.7$, $p_T > 6$ GeV. If the separation between a muon and any jet is $\Delta R < 0.4$, the muon is omitted.

---

[3] For the overlap removal, rapidity is used instead of pseudorapidity in the ΔR definition.

The $\mathbf{p}_T^{miss}$ is the negative vector sum of the p_T of all selected and calibrated physics objects in the event. An extra term is added to account for small energy depositions in the event that are not associated to any of the selected objects. This "soft" term is calculated from inner detector tracks with $p_T > 400$ MeV matched to the primary vertex, to make it resilient to pileup contamination, not associated with physics objects [62]. The missing transverse momentum from the tracking system (denoted as $\mathbf{p}_T^{miss,track}$, with magnitude $E_T^{miss,track}$) is computed from the vector sum of the reconstructed inner detector tracks with $p_T > 500$ MeV, $|\eta| < 2.5$, that are associated with the primary vertex in the event.

The requirements on electrons and muons are tightened for the selection of events in background control regions (described in section 7) containing leptons. Electron and muon candidates are required to have $p_T > 20$ GeV ($p_T > 28$ GeV) for regions using the E_T^{miss} (lepton) triggers and to satisfy p_T-dependent track- and calorimeter-based isolation criteria. Electron candidates are required to pass a "tight" likelihood-based selection. The impact parameter of the electron in the transverse plane with respect to the reconstructed event primary vertex ($|d_0|$) is required to be less than five times the impact parameter uncertainty (σ_{d0}). The impact parameter along the beam direction, $|z_0 \times \sin\theta|$, is required to be less than 0.5 mm. Further selection criteria on reconstructed muons are also imposed: muon candidates are required to pass a "medium" quality selection [63]. In addition, the requirements $|d_0| < 3\sigma_{d_0}$ and $|z_0 \times \sin\theta| < 0.5$ mm are imposed for muon candidates.

6 Signal region definitions

The main experimental signature for all signal topologies is the presence of multiple jets (two of which contain b-hadrons), no muons or electrons, and significant missing transverse momentum.

Five sets of signal regions (SRA-E) are defined to target each topology and kinematic regime. SRA (SRB) is sensitive to production of high-mass $\tilde{t}$ pairs with large (intermediate) $\Delta m(\tilde{t}, \tilde{\chi}_1^0)$. Both SRA and SRB employ top-mass reconstruction techniques to reject background. SRC is designed for the highly compressed region with $\Delta m(\tilde{t}, \tilde{\chi}_1^0) \sim m_t$. In this signal region, initial-state radiation (ISR) is used to improve sensitivity to these decays. SRD is targeted at $\tilde{t} \to b\tilde{\chi}_1^\pm$ decays, where no top-quark candidates are reconstructed. SRE is optimized for scenarios with highly-boosted top quarks that can occur in gluino-mediated top-squark production.

A common preselection is defined for all signal regions. At least four jets are required, at least one of which must be b-tagged. The leading four jets (ordered in p_T) must satisfy $p_T^0, p_T^1, p_T^2, p_T^3 > 80, 80, 40, 40$ GeV due to the tendency for signal events to have more energetic jets than background. Events containing reconstructed electrons or muons are vetoed. The E_T^{miss} trigger threshold motivates the requirement $E_T^{miss} > 250$ GeV and rejects the majority of background from multijet and all-hadronic $t\bar{t}$ events. In order to reject events with mis-measured E_T^{miss} originating from multijet and hadronic $t\bar{t}$ decays, an angular separation between the azimuthal angle of the two highest-p_T jets and the E_T^{miss} is required: $\left|\Delta\phi\left(\text{jet}^{0,1}, \mathbf{p}_T^{miss}\right)\right| > 0.4$. Further reduction of such events is achieved by requiring the $E_T^{miss,track}$ to be aligned in ϕ with respect to the E_T^{miss} calculated from the calorimeter system: $E_T^{miss,track} > 30$ GeV and $\left|\Delta\phi\left(\mathbf{p}_T^{miss}, \mathbf{p}_T^{miss,track}\right)\right| < \pi/3$ radians.
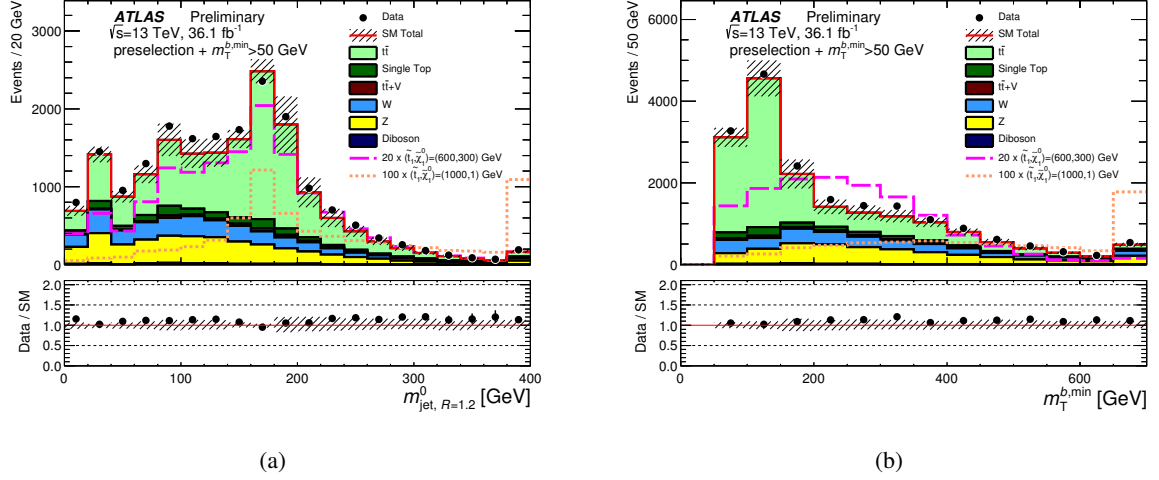
Figure 2: Distributions of the discriminating variables (a) $m_{\text{jet}, R=1.2}^0$ and (b) $m_{\text{T}}^{b,\min}$ after the common preselection and an additional $m_{\text{T}}^{b,\min} > 50$ GeV requirement. The stacked histograms show the SM expectation before being normalized using scale factors derived from the simultaneous fit to all backgrounds. The "Data/SM" plots show the ratio of data events to the total SM expectation. The hatched uncertainty band around the SM expectation and in the ratio plots illustrates the combination of statistical and detector-related systematic uncertainties. The rightmost bin includes all overflows.

Signal Regions A and B

SRA and SRB are targeted at direct top-squark pair production where the top squarks decay via $\tilde{t} \to t\tilde{\chi}_1^0$ with $\Delta m(\tilde{t}, \tilde{\chi}_1^0) > m_t$. SRA is optimized for $m_{\tilde{t}} = 1000$ GeV, $m_{\tilde{\chi}^0} = 1$ GeV while SRB is optimized for $m_{\tilde{t}} = 600$ GeV, $m_{\tilde{\chi}^0} = 300$ GeV. Two b-tagged jets ($N_{b-\text{jet}}$) are required and an additional requirement on the $\Delta\phi$ of the three leading jets and the $E_{\text{T}}^{\text{miss}}$ of $\left| \Delta\phi\left(\text{jet}^{0,1,2}, \mathbf{p}_{\text{T}}^{\text{miss}} \right) \right| > 0.4$ is made in SRA and SRB.

The decay products of the $t\bar{t}$ system in the all-hadronic decay mode can often be reconstructed as six distinct $R = 0.4$ jets. The transverse shape of these jets is typically circular with a radius equal to this distance parameter, but when two of the jets are less than $2R$ apart in $\eta - \phi$ space, the one-to-one correspondence of a jet with a top daughter may no longer hold. Thus, the two hadronic top candidates are reconstructed by applying the anti-k_t clustering algorithm [52] to the $R = 0.4$ jets, using reclustered distance parameters of $R = 0.8$ and $R = 1.2$. Two $R = 1.2$ reclustered jets are required; the mass of the highest-p_{T} $R = 1.2$ reclustered jet is shown in Fig. 2 (a). The events are divided into three categories based on the resulting $R = 1.2$ reclustered jet masses ordered in p_{T}, as illustrated in Fig. 3: the "TT" category includes events with two top candidates i.e. with masses $m_{\text{jet}, R=1.2}^0 > 120$ GeV and $m_{\text{jet}, R=1.2}^1 > 120$ GeV, the "TW" category contains events with one top candidate and a W candidate i.e. where $m_{\text{jet}, R=1.2}^0 > 120$ GeV and $60 < m_{\text{jet}, R=1.2}^1 < 120$ GeV, and the "T0" category represents events with only one top candidate, i.e. where $m_{\text{jet}, R=1.2}^0 > 120$ GeV and $m_{\text{jet}, R=1.2}^1 < 60$ GeV. Since the signal-to-background ratio is quite different in each of these categories, they are optimized individually for both SRA and SRB.

The most powerful discriminating variable against SM $t\bar{t}$ production is the $E_{\text{T}}^{\text{miss}}$ resulting from the undetected $\tilde{\chi}_1^0$s. Substantial $t\bar{t}$ background rejection is provided by additional requirements to reject
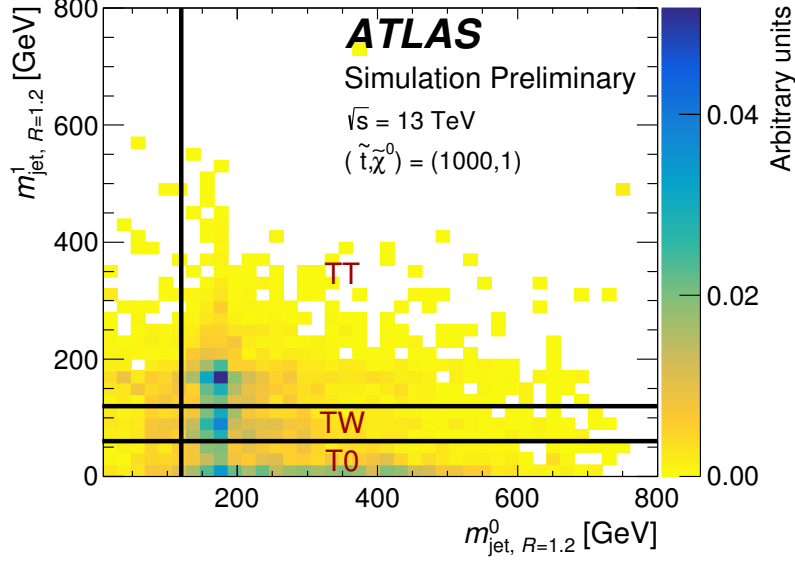
Figure 3: Illustration of signal-region categories (TT, TW, and T0) based on the $R = 1.2$ reclustered top-candidate masses for simulated direct top-squark pair production with $(m_{\tilde{t}}, m_{\tilde{\chi}_1^0}) = (1000, 1)$ GeV after the loose preselection requirement described in the text. The black lines represent the requirements on the reclustered jet masses.

events in which one W decays via a charged lepton plus neutrino. The first requirement is that the transverse mass (m_{T}) calculated from the $E_{\mathrm{T}}^{\mathrm{miss}}$ and the b-tagged jet with minimum distance in ϕ to the $\mathbf{p}_{\mathrm{T}}^{\mathrm{miss}}$ direction is above 200 GeV:

$$m_{\mathrm{T}}^{b,\mathrm{min}} = \sqrt{2\, p_{\mathrm{T}}^b\, E_{\mathrm{T}}^{\mathrm{miss}} \left[1 - \cos \Delta\phi \left(\mathbf{p}_{\mathrm{T}}^b, \mathbf{p}_{\mathrm{T}}^{\mathrm{miss}} \right) \right]} > 200 \ \mathrm{GeV}, \tag{1}$$

which is bounded to be below the top quark mass, as illustrated in Fig. 2 (b). An additional requirement is made on the mass of the leading (in p_{T}) $R=0.8$ reclustered jet to be consistent with a W candidate: $m_{\mathrm{jet}, R=0.8}^0 > 60$ GeV. Additionally, requirements on the stransverse mass ($m_{\mathrm{T2}}^{\chi^2}$) [64, 65] are made which are especially powerful in the T0 category where a χ^2 method is applied to reconstruct top quarks with lower momenta where reclustering was suboptimal. The $m_{\mathrm{T2}}^{\chi^2}$ variable is constructed from the direction and magnitude of the $E_{\mathrm{T}}^{\mathrm{miss}}$ in the transverse plane as well as the direction of two top quark candidates reconstructed using a χ^2 method. The minimization of the method is done in terms of $\chi^2 = \frac{(m_{\mathrm{cand}} - m_{\mathrm{true}})^2}{m_{\mathrm{true}}}$, where m_{cand} is the candidate mass and m_{true} is set to 80.4 GeV for W candidates and 173.2 GeV for top candidates. Initially pairs of $R = 0.4$ jets form W candidates which are then used to construct top candidates using additional $R = 0.4$ jets in the event. The top candidates selected by the χ^2 method are only used for the momenta in $m_{\mathrm{T2}}^{\chi^2}$ while the hypothesis masses for the top quarks and the invisible particles are set to 173.2 GeV and 0 GeV, respectively. Finally, a "τ-veto" requirement is applied to reject hadronic τ-lepton candidates likely to have originated from a $W \to \tau\nu$ decay. Here, events that contain a non-b-tagged jet within $|\eta| < 2.5$ with fewer than four associated charged-particle tracks with $p_{\mathrm{T}} > 500$ MeV, and where the $\Delta\phi$ between the jet and the $\mathbf{p}_{\mathrm{T}}^{\mathrm{miss}}$ is less than $\pi/5$ radians, are vetoed. In SRB, additional discrimination is provided by $m_{\mathrm{T}}^{b,\mathrm{max}}$ and $\Delta R(b, b)$. The former quantity is analogous to $m_{\mathrm{T}}^{b,\mathrm{min}}$ except that the transverse mass is computed with the b-tagged jet that has the largest $\Delta\phi$ with

respect to the $\mathbf{p}_T^{\text{miss}}$ direction. The latter quantity provides additional discrimination against background where the two b-tagged jets come from a gluon splitting. Table 1 summarizes the selection criteria that are used in these two signal regions.

Table 1: Selection criteria for SRA and SRB, in addition to the common preselection requirements described in the text. The signal regions are separated into topological categories based on reconstructed top-candidate masses.

Signal Region			TT	TW	T0
	$m_{\text{jet}, R=1.2}^0$			> 120 GeV	
	$m_{\text{jet}, R=1.2}^1$		> 120 GeV	[60, 120] GeV	< 60 GeV
	$m_T^{b,\min}$			> 200 GeV	
	$N_{b-\text{jet}}$			≥ 2	
	τ-veto			yes	
	$\left\lvert \Delta\phi\left(\text{jet}^{0,1,2}, \mathbf{p}_T^{\text{miss}}\right)\right\rvert$			> 0.4	
A	$m_{\text{jet}, R=0.8}^0$			> 60 GeV	
	$\Delta R\,(b, b)$		> 1	-	
	$m_{\text{T2}}^{\chi^2}$		> 400 GeV	> 400 GeV	> 500 GeV
	E_T^{miss}		> 400 GeV	> 500 GeV	> 550 GeV
B	$m_T^{b,\max}$			> 200 GeV	
	$\Delta R\,(b, b)$			> 1.2	

Signal Regions C

SRC is optimized for direct top-squark pair production where $\Delta m(\tilde{t}, \tilde{\chi}_1^0) \approx m_t$, a regime in which the signal topology is very similar to SM $t\bar{t}$ production. In the presence of high-momentum ISR, which can be reconstructed as multiple jets and form an ISR system, the di-top-squark system is boosted in the transverse plane. The ratio of the E_T^{miss} to the p_T of the ISR system in the centre-of-mass (CM) frame (p_T^{ISR}), defined as R_{ISR}, is proportional to the ratio of the $\tilde{\chi}_1^0$ and $\tilde{t}$ masses [66, 67]:

$$R_{\text{ISR}} \equiv \frac{E_T^{\text{miss}}}{p_T^{\text{ISR}}} \sim \frac{m_{\tilde{\chi}_1^0}}{m_{\tilde{t}}}. \tag{2}$$

A recursive jigsaw reconstruction technique, as described in Ref. [68], is used to divide each event into an ISR hemisphere and a sparticle hemisphere, where the latter consists of the pair of candidate top squarks, each of which decays via a top quark and a $\tilde{\chi}_1^0$. Objects are grouped together based on their proximity in the lab frame's transverse plane by minimizing the reconstructed transverse masses of the ISR system and sparticle system simultaneously over all choices of object assignment. Kinematic variables are then defined based on this assignment of objects to either the ISR system or the sparticle system. This method

is equivalent to dividing the event according to the axis of maximum back-to-back p_T in the event's CM frame where the total p_T of all accepted objects sum to zero. In events with strong ISR, the axis of maximum back-to-back p_T, also known as the thrust axis, should approximate the direction of the ISR and sparticles' back-to-back recoil.

The selection criteria for this signal region are summarized in Table 2. The events are divided into five windows defined by non-overlapping ranges of the reconstructed R_{ISR}, and target different top squark and $\tilde{\chi}_1^0$ masses: e.g., SRC2 is optimized for $m_{\tilde{t}} = 300$ GeV, $m_{\tilde{\chi}^0} = 127$ GeV and SRC4 is optimized for $m_{\tilde{t}} = 500$ GeV, $m_{\tilde{\chi}^0} = 327$ GeV. Five jets or more are required to be assigned to the sparticle hemisphere of the event (N_{jet}^S), and at least one of those jets (N_{b-jet}^S) must be b-tagged. Transverse-momentum requirements on p_T^{ISR}, the highest-p_T b-jet in the sparticle hemisphere ($p_{T,b}^{0,S}$), and the fourth-highest-p_T jet in the sparticle hemisphere ($p_T^{4,S}$) are applied. The transverse mass between the entire sparticle system (include the invisible part) and the E_T^{miss}, defined as m_S, is required to be > 300 GeV. The ISR system is also required to be separated in azimuth from the E_T^{miss} in the CM frame; this variable is defined as $\Delta\phi_{ISR,E_T^{miss}}$.

Table 2: Selection criteria for SRC, in addition to the common preselection requirements described in the text. The signal regions are separated into windows based on ranges of R_{ISR}.

Variable	SRC1	SRC2	SRC3	SRC4	SRC5
N_{b-jet}	≥ 1				
N_{b-jet}^S	≥ 1				
N_{jet}^S	≥ 5				
$p_{T,b}^{0,S}$	> 40 GeV				
m_S	> 300 GeV				
$\Delta\phi_{ISR,E_T^{miss}}$	> 3.0				
p_T^{ISR}	> 400 GeV				
$p_T^{4,S}$	> 50 GeV				
R_{ISR}	0.30-0.40	0.40-0.50	0.50-0.60	0.60-0.70	0.70-0.80

Signal Regions D

SRD is optimized for direct top-squark pair production where both top squarks decay via $\tilde{t} \to b\tilde{\chi}_1^\pm$ where $m_{\tilde{\chi}_1^\pm} = 2m_{\tilde{\chi}^0}$. In this signal region, at least five jets are required, two of which must be b-tagged. The sum of the p_Ts of the two jets with the highest b-tagging weight ($p_T^{0,b} + p_T^{1,b}$) as well as the second (p_T^1), fourth (p_T^3), and fifth (p_T^4) jet p_Ts are used for additional background rejection. SRD-low and SRD-high are optimized for $m_{\tilde{t}} = 400$ GeV, $m_{\tilde{\chi}^0} = 50$ GeV and $m_{\tilde{t}} = 700$ GeV, $m_{\tilde{\chi}^0} = 100$ GeV, respectively. The models considered for the optimization have $m(\tilde{\chi}_1^\pm) = 2m(\tilde{\chi}_1^0)$. Tighter leading and sub-leading jet p_T requirements are made for SRD-high, as summarized in Table 3.

Table 3: Selection criteria for SRD, in addition to the common preselection requirements described in the text.

Variable	SRD-low	SRD-high
$\left\|\Delta\phi\left(\text{jet}^{0,1,2}, \mathbf{p}_T^{\text{miss}}\right)\right\|$	> 0.4	
$N_{b-\text{jet}}$	≥2	
$\Delta R\left(b, b\right)$	> 0.8	
$p_T^{0,b} + p_T^{1,b}$	> 300 GeV	> 400 GeV
τ-veto	yes	
p_T^1	> 150 GeV	
p_T^3	> 100 GeV	> 80 GeV
p_T^4	> 60 GeV	
$m_T^{b,\text{min}}$	> 250 GeV	> 350 GeV
$m_T^{b,\text{max}}$	> 300 GeV	> 450 GeV

Signal Region E

SRE is designed for models which have highly-boosted top quarks. Such signatures can arise from direct pair production of high-mass top partners, or from the gluino-mediated compressed $\tilde{t}$ scenario with large $\Delta m(\tilde{g}, \tilde{t})$. In this regime, reclustered jets with $R = 0.8$ are utilized to optimize experimental sensitivity to these highly-boosted top quarks. In this signal region, at least four jets are required, two of which must be b-tagged. Additional discrimination is provided by a measure of the E_T^{miss} significance: $E_T^{\text{miss}}/\sqrt{H_T}$, where H_T is the scalar sum of the p_T of all reconstructed $R = 0.4$ jets in an event. The selection criteria for SRE, optimized for $m_{\tilde{g}} = 1700$ GeV, $m_{\tilde{t}} = 400$ GeV, $m_{\tilde{\chi}^0} = 395$ GeV, are summarized in Table 4.

7 Background estimation

The main SM background process in SRA, SRB, SRD, and SRE is $Z \to \nu\bar{\nu}$ production in association with heavy flavor jets. The second most dominant background is $t\bar{t}$ production where one W decays via a lepton and neutrino and the lepton (particularly a hadronically decaying τ lepton) is either not identified or is reconstructed as a jet. This process is the major background contribution in SRC and an important background in SRB, SRD and SRE as well. Other important background processes are $W \to \ell\nu$ plus heavy flavor jets, single top and the irreducible background from $t\bar{t} + Z$, where the Z decays to two neutrinos.

The main background contributions are estimated primarily from comparisons between data and simulation outside the signal regions. Control regions (CRs) are designed to enhance a particular background process, and are orthogonal to the SRs while probing a similar event topology. The CRs are used to normalize the simulation to data, but extrapolation from the CR to the SR are taken from simulation. Sufficient

Table 4: Selection criteria for SRE in addition to the common preselection requirements described in the text.

Variable	SRE
$\left\vert\Delta\phi\left(\text{jet}^{0,1,2},\mathbf{p}_\text{T}^\text{miss}\right)\right\vert$	> 0.4
$N_{b-\text{jet}}$	≥ 2
$m^0_{\text{jet},R=0.8}$	> 120 GeV
$m^1_{\text{jet},R=0.8}$	> 80 GeV
$m_\text{T}^{b,\min}$	> 200 GeV
E_T^miss	> 550 GeV
H_T	> 800 GeV
$E_\text{T}^\text{miss}/\sqrt{H_\text{T}}$	$> 18\sqrt{\text{GeV}}$

data are needed to avoid large statistical uncertainties in the background estimates, and the CR definitions are chosen to be kinematically as close as possible to all SRs, to minimize the systematic uncertainties associated with extrapolating the background yield from the CR to the SR. Where CR definitions are farther from the SR definition, validation regions are employed to cross-check the extrapolation. In addition, control-region selection criteria are chosen to minimize potential contamination from signal that could shadow contributions in the signal regions. The signal contamination is below 8% in all CRs for all signal points that have not been excluded by previous ATLAS searches. As the CRs are not 100% pure in the process of interest, the cross-contamination between CRs from other processes is estimated. The normalization factors and the cross contamination are determined simultaneously for all regions using a fit described below.

Detailed CR definitions are given in Tables 5, 6, and 7 and are defined by the presence of one or more leptons that make them orthogonal with the signal regions. The $\left\vert\Delta\phi\left(\text{jet}^{0,1,2},\mathbf{p}_\text{T}^\text{miss}\right)\right\vert$ and $m_\text{T}(\ell, E_\text{T}^\text{miss})$ requirements are designed to reduce contamination from SM multijet processes. The number of leptons is indicated by N_ℓ and the transverse momentum of the lepton is indicated by p_T^ℓ. In all one-lepton CRs, once the trigger and minimum p_T^ℓ selection are applied, the lepton is treated as a non-b-tagged jet (to emulate the hadronic τ decays in the SRs) in the computation of all jet-related variables. In the two-lepton CRZs, a lepton-p_T requirement of at least 28 GeV is made to be fully efficient for the trigger selection. The invariant mass of the two oppositely-charged leptons, indicated by $m_{\ell\ell}$, is selected to be consistent with the leptons having originated from a Z. The transverse momenta of these leptons are then vectorially added to the $\mathbf{p}_\text{T}^\text{miss}$ to mimic the $Z \to \nu\bar{\nu}$ decays in the SRs, forming the quantity $E_\text{T}^{\text{miss}'}$. Quantities that depend on the E_T^miss are recalculated in the CRZs using $E_\text{T}^{\text{miss}'}$ and identified by the addition of a prime (e.g. $m_\text{T}^{b,\min'}$ and $m_\text{T}^{b,\max'}$). Requirements such as the maximum $m_\text{T}(\ell, E_\text{T}^\text{miss})$ and the minimum ΔR between the two highest-weight b-tagged jets and the lepton, $\Delta R (b, \ell)_\text{min}$, are used to enforce orthogonality. In CRST, the requirement on the ΔR between the two highest-weight b-tagged jets, $\Delta R (b, b)$, is used to reject $t\bar{t}$ contamination from the control region enriched in single-top events. Finally, the normalization of the $t\bar{t}+W/Z$ background in the signal region, which is completely dominated by $t\bar{t} + Z(\to \nu\nu)$, is estimated with a $t\bar{t} + \gamma$ control region (CRTTGamma). The same lepton triggers and lepton-p_T requirements are made as in the CRZs. Additionally, the presence of a photon with $p_\text{T} > 150$ GeV is required which is

used to model the Z decay in the signal regions due to the similarity between the diagrams for photons and Z production. Similar to the Z control region, the photon is used in the estimation of E_T^{miss} related variables.

To estimate the Z + jets and $t\bar{t}$ background in the different kinematic regions of the signal regions, individual control regions are designed for all signal regions where possible. Only if the statistical power of control regions is low, are they merged to form one control region for multiple signal regions. In the case of CRST, CRW, and CRTTGamma this results in the use of one common CR for all signal regions. Distributions from the Z + jets, $t\bar{t}$, W + jets, single top, and $t\bar{t}\gamma$ control regions (CRZs, CRTs, CRST, CRW, and CRTTGamma, respectively) are shown in Figure 4.

Table 5: Selection criteria for the Z + jets control regions used to estimate the Z + jets background contributions in the signal regions.

Selection	CRZAB-TT-TW	CRZAB-T0	CRZD	CRZE
Trigger	electron (muon)			
N_ℓ	2, same flavor			
p_T^ℓ	> 28 GeV			
$m_{\ell\ell}$	[86,96] GeV			
N_{jet}	≥ 4			
$p_T^0, p_T^1, p_T^2, p_T^3$	$80, 80, 40, 40$ GeV			
E_T^{miss}	< 50 GeV			
$E_T^{\mathrm{miss}'}$	> 100 GeV			
$N_{b-\mathrm{jet}}$	≥ 2			
$m_{\mathrm{jet},R=1.2}^0$	> 120 GeV		-	
$m_{\mathrm{jet},R=1.2}^1$	> 60 GeV	< 60 GeV	-	
$m_T^{b,\mathrm{min}'}$	-		> 200 GeV	
$m_T^{b,\mathrm{max}'}$	-		> 200 GeV	-
H_T	-			> 500 GeV

Table 6: Selection criteria for the $t\bar{t}$ control regions used to estimate the $t\bar{t}$ background contributions in the signal regions.

Selection	CRTA-TT	CRTA-TW	CRTA-T0	CRTB-TT	CRTB-TW	CRTB-T0	CRTC	CRTD	CRTE
Trigger	E_T^{miss}								
N_ℓ	1								
p_T^ℓ	> 20 GeV								
N_{jet}	≥ 4 (including lepton)								
$p_T^0, p_T^1, p_T^2, p_T^3$	80, 80, 40, 40 GeV								
N_{b-jet}	≥ 2								
$\left\|\Delta\phi\left(jet^{0,1}, \mathbf{p}_T^{miss}\right)\right\|$	> 0.4								
$\left\|\Delta\phi\left(jet^{0,1,2}, \mathbf{p}_T^{miss}\right)\right\|$	> 0.4	> 0.4	> 0.4	> 0.4	> 0.4	> 0.4	-	> 0.4	> 0.4
$m_T(\ell, E_T^{miss})$	[30, 100] GeV	[30, 100] GeV	[30, 100] GeV	[30, 100] GeV	[30, 100] GeV	[30, 100] GeV	< 100 GeV	[30, 100] GeV	[30, 100] GeV
$m_T^{b,min}$	> 100 GeV	> 100 GeV	> 100 GeV	> 100 GeV	> 100 GeV	> 100 GeV	-	> 100 GeV	> 100 GeV
$\Delta R(b, \ell)_{min}$	< 1.5	< 1.5	< 1.5	< 1.5	< 1.5	< 1.5	< 2.0	< 1.5	< 1.5
$m_{jet, R=1.2}^0$	> 120 GeV	> 120 GeV	> 120 GeV	> 120 GeV	> 120 GeV	> 120 GeV	-	-	-
$m_{jet, R=1.2}^1$	> 120 GeV	[60, 120] GeV	< 60 GeV	> 120 GeV	[60, 120] GeV	< 60 GeV	-	-	-
$m_{jet, R=0.8}^0$	> 60 GeV	> 60 GeV	> 60 GeV	-	-	-	-	-	> 120 GeV
$m_{jet, R=0.8}^1$	> 60 GeV	> 60 GeV	> 60 GeV	-	-	-	-	-	> 80 GeV
E_T^{miss}	> 250 GeV	> 300 GeV	> 350 GeV	> 250 GeV	> 250 GeV	> 250 GeV	> 250 GeV	> 250 GeV	> 250 GeV
$\Delta R(b, b)$	> 1.0	-	-	-	> 1.2	> 1.2	-	> 0.8	-
$m_T^{b,max}$	-	-	-	-	> 200 GeV	> 200 GeV	-	> 100 GeV	-
p_T^1	-	-	-	-	-	-	-	> 150 GeV	-
p_T^3	-	-	-	-	-	-	-	> 80 GeV	-
$p_T^{0,b} + p_T^{1,b}$	-	-	-	-	-	-	-	> 300 GeV	-
N_{jet}^S	-	-	-	-	-	-	≥ 5	-	-
N_{b-tag}^S	-	-	-	-	-	-	≥ 1	-	-
p_T^{ISR}	-	-	-	-	-	-	> 400 GeV	-	-
$p_T^{4,S}$	-	-	-	-	-	-	> 40 GeV	-	-
H_T	-	-	-	-	-	-	-	-	> 500 GeV

Table 7: Selection criteria for the common W + jets, single-top, and $t\bar{t} + \gamma$ control-region definitions.

Selection	CRW	CRST	CRTTGamma
Trigger	$E_{\mathrm{T}}^{\mathrm{miss}}$		lepton
N_ℓ	1		
p_{T}^ℓ	> 20 GeV		> 28 GeV
N_γ	-		1
p_{T}^γ	-		> 150 GeV
N_{jet}	$\geq$ 4 (including lepton)		$\geq$ 4
$p_{\mathrm{T}}^0, p_{\mathrm{T}}^1, p_{\mathrm{T}}^2, p_{\mathrm{T}}^3$	80, 80, 40, 40 GeV		
$N_{b-\mathrm{jet}}$	1	$\geq$ 2	
$\left\| \Delta\phi\left(\mathrm{jet}^{0,1}, \mathbf{p}_{\mathrm{T}}^{\mathrm{miss}}\right)\right\|$	> 0.4		-
$m_{\mathrm{T}}(\ell, E_{\mathrm{T}}^{\mathrm{miss}})$	[30, 100] GeV		-
$\Delta R\,(b, \ell)_{\mathrm{min}}$	> 2.0		-
$E_{\mathrm{T}}^{\mathrm{miss}}$	> 250 GeV		-
$\Delta R\,(b, b)$	-	> 1.5	-
$m_{\mathrm{jet}, R=1.2}^0$	< 60 GeV	> 120 GeV	-
$m_{\mathrm{T}}^{b,\mathrm{min}}$	-	> 200 GeV	-

Contributions from all-hadronic $t\bar{t}$ and multijet production are found to be negligible. These are estimated from data using a procedure described in detail in Ref. [69]. The procedure determines the jet response from simulated dijet events, and then uses this response function to smear the jet response in low-$E_{\mathrm{T}}^{\mathrm{miss}}$ seed events. The jet response is cross-checked with data where the $E_{\mathrm{T}}^{\mathrm{miss}}$ can be unambiguously attributed to the mis-measurement of one of the jets. Diboson production, which is also sub-dominant, is estimated directly from simulation.

Simultaneous fit to determine SM background

The observed numbers of events in the various control regions are included in a profile likelihood fit [70] to determine the SM background estimates in each signal region. A likelihood function is built as the product of Poisson probability functions, describing the observed and expected number of events in the control regions [71]. This procedure takes common systematic uncertainties (discussed in detail in Section 8) between the control and signal regions and their correlations into account as they are treated as nuisance parameters in the fit and are modelled by Gaussian probability density functions. The contributions from all other background processes are fixed at the values expected from the simulation, using the most accurate theoretical cross sections available, as described in Section 4, while their uncertainties are used as nuisance parameters in the fit.
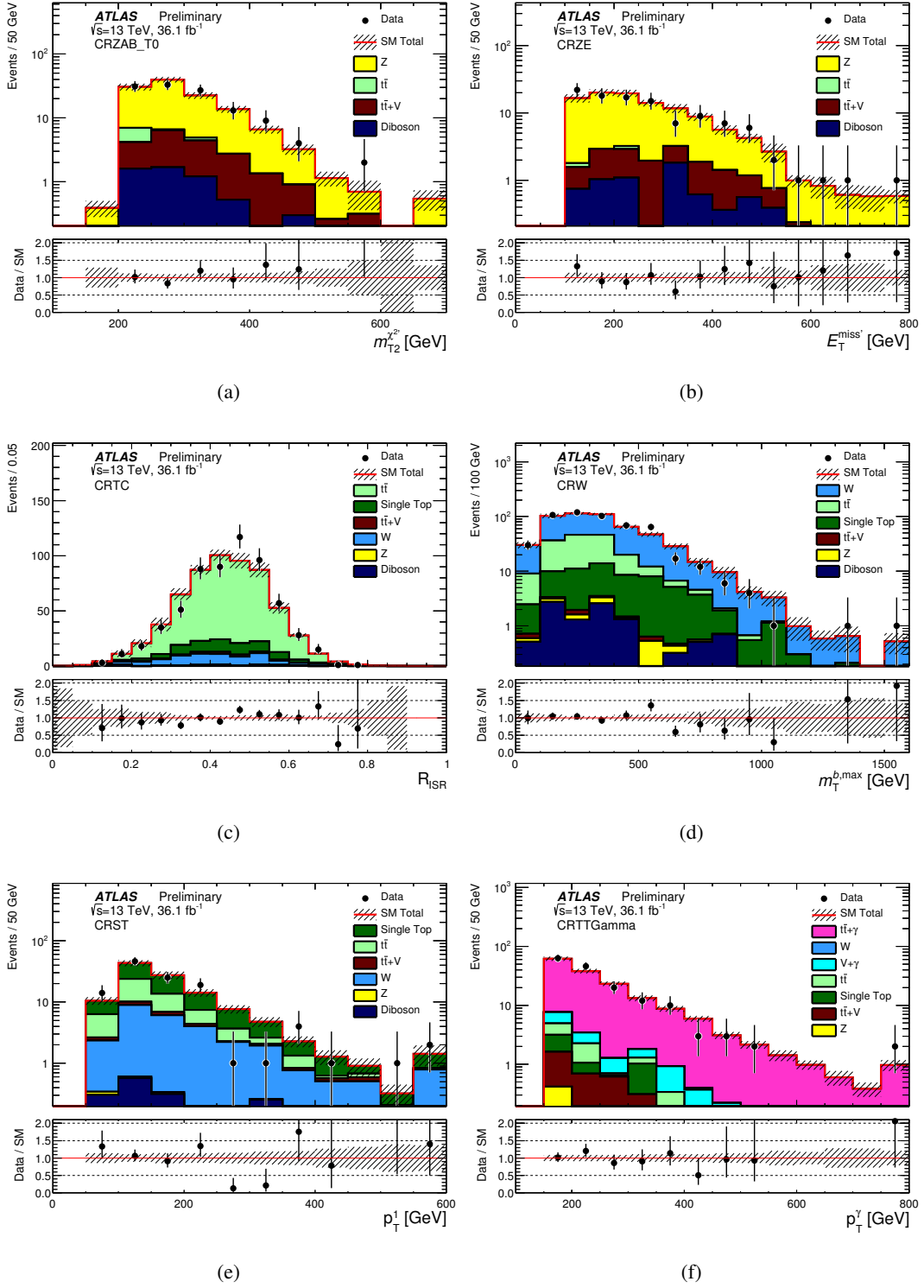
Figure 4: (a) $m_{\mathrm{T2}}^{\chi^2}$ distribution in CRZAB-T0, (b) $E_{\mathrm{T}}^{\mathrm{miss}'}$ in CRZE , (c) the R_{ISR} distribution in CRTC, (d) the $m_{\mathrm{T}}^{b,\mathrm{max}}$ distribution in CRW, (e) the transverse momentum of the second-leading-p_{T} jet in CRST, and (f) the photon p_{T} distribution in CRTTGamma. The stacked histograms show the SM expectation, normalized using scale factors derived from the simultaneous fit to all backgrounds. The "Data/SM" plots show the ratio of data events to the total SM expectation. The hatched uncertainty band around the SM expectation and in the ratio plot illustrates the combination of MC statistical and detector-related systematic uncertainties. The rightmost bin includes all overflows.

Zero lepton VRs (VRZAB, VRZD, VRZE) are designed to validate the background estimate for Z + jets in the signal regions. No VRZ is designed for SRC due to the negligible contribution of the Z background in this region. The definitions of the VRZs, after the common zero-lepton preselection discussed in Section 6 are applied, are shown in Table 8. To provide orthogonality to the signal regions, the requirement on one or more of the following variables is inverted: $\Delta R\,(b, b)$, $m^0_{\mathrm{jet},\,R=1.2}$, $m^0_{\mathrm{jet},\,R=0.8}$.

To validate the $t\bar{t}$ background, zero-lepton VRs sharing the same common preselection of the signal regions and which are close to SRA and SRB definitions are designed for each of the categories (VRTA-TT, VRTA-TW, VRTA-T0, VRTB-TT, VRTB-TW, VRTB-T0). To avoid overlap with the signal regions the $m^{b,\min}_{\mathrm{T}}$ requirement is inverted in all validation regions. In VRTA, SRA requirements remain unchanged except for $m^{\chi^2}_{\mathrm{T2}}$ not being applied, $100 < m^{b,\min}_{\mathrm{T}} < 200$ GeV, and the $E^{\mathrm{miss}}_{\mathrm{T}}$ requirement being reduced by 100 GeV. For VRTB, all requirements in the VRs are the same as in the SRs except for the $m^{b,\min}_{\mathrm{T}}$ which is $100 < m^{b,\min}_{\mathrm{T}} < 200$ GeV for VRTB-TT, $140 < m^{b,\min}_{\mathrm{T}} < 200$ GeV for VRTB-TW, and $160 < m^{b,\min}_{\mathrm{T}} < 200$ GeV for VRTB-T0. For SRC, the same requirements are used when defining the validation region (VRTC) except for the looser requirements of $m_{\mathrm{S}} > 100$ GeV, $p^{4,\mathrm{S}}_{\mathrm{T}} > 40$ GeV and $N^{\mathrm{S}}_{\mathrm{jet}} > 4$. The $\Delta\phi_{\mathrm{ISR},E^{\mathrm{miss}}_{\mathrm{T}}}$ requirement is inverted and $m_{\mathrm{V}}/m_{\mathrm{S}} < 0.6$, where m_{V} is the transverse mass between the visible objects of the sparticle system and the $E^{\mathrm{miss}}_{\mathrm{T}}$, is applied in addition to the existing selection. The validation region to validate the background estimates in SRD (VRTD) is formed by applying the following requirements: $100 < m^{b,\min}_{\mathrm{T}} < 200$ GeV, $p^{0,b}_{\mathrm{T}} + p^{1,b}_{\mathrm{T}} > 300$ GeV, $p^3_{\mathrm{T}} > 80$ GeV, and $m^{b,\max}_{\mathrm{T}} > 300$ GeV. All other requirements are applied exactly as in SRD-low except for the requirement on p^4_{T} which is dropped. Finally, the validation region defined for SRE (VRTopE) applies only the same requirements on the number of b-jets, $m^0_{\mathrm{jet},\,R=0.8}$, and $m^1_{\mathrm{jet},\,R=0.8}$, inverting the $m^{b,\min}_{\mathrm{T}}$ requirement to $100 < m^{b,\min}_{\mathrm{T}} < 200$ GeV. No other requirement is applied to VRTE.

One one-lepton validation region for the W + jets background (VRW) is used to test the W background estimates in all SRs. In this case the validation region is designed based on the definition of CRW. Compared to CRW, the requirement that differs is $\Delta R(b_{0,1}, \ell)_{\min}$ which is greater than 1.8 for the validation region. Two additional requirements are included in the definition of VRW, namely $m^{b,\min}_{\mathrm{T}} > 150$ GeV and $m^0_{\mathrm{jet},\,R=1.2} < 70$ GeV.

The result of the simultaneous fit procedure for each VR is shown in Figure 5 which displays good agreement between data and MC predictions.

8 Systematic uncertainties

Experimental and theoretical systematic uncertainties in the SM expectations and signal expectations are included in the profile likelihood fit described in Section 7.

The dominant uncertainty to all SRs except for SRB is the statistical uncertainty on the mean estimate of the total background contribution. The main sources of detector-related systematic uncertainties in the SM background estimates originate from the jet energy scale (JES) and jet energy resolution (JER), b-tagging efficiency, $E^{\mathrm{miss}}_{\mathrm{T}}$ soft term, and pileup. The effect of the JES and JER uncertainties on the background estimates in the signal regions reaches up to 16%. The uncertainty on the b-tagging efficiency is no more than 9%. All jet- and lepton-related uncertainties are propagated to the calculation of the $E^{\mathrm{miss}}_{\mathrm{T}}$, and additional uncertainties on the energy and resolution of the soft term are also included. The uncertainty on the soft term of the $E^{\mathrm{miss}}_{\mathrm{T}}$ is most significant in SRA-T0 at 6%. An uncertainty due to the pileup modeling

Table 8: Selection criteria for the Z validation regions used to validate the Z background estimates in the signal regions.

Selection	VRZAB	VRZD	VRZE
Jet p_T^0, p_T^1	80, 80 GeV	150, 80 GeV	80, 80 GeV
N_{jet}	≥ 4	≥ 5	≥ 4
N_{b-jet}	≥ 2		
τ-veto	yes		no
$m_T^{b,min}$	> 200 GeV		
$m_{jet,R=1.2}^0$	< 120 GeV	-	
$\Delta R\,(b,b)$	< 1.0	< 0.8	< 1.0
$m_T^{b,max}$	-	> 200 GeV	-
H_T	-		> 500 GeV
$E_T^{miss}/\sqrt{H_T}$	-		> 14 $\sqrt{\text{GeV}}$
$m_{jet,R=0.8}^0$	-		< 120 GeV

is also considered with a contribution up to 14%. Lepton reconstruction and identification uncertainties are also considered but have a small impact.

The preliminary uncertainty on the combined 2015+2016 integrated luminosity is 3.2%. It is derived, following a methodology similar to that detailed in Ref. [28], from a preliminary calibration of the luminosity scale using x-y beam-separation scans performed in August 2015 and May 2016.

Theoretical uncertainties in the modelling of the SM background are evaluated. For the W/Z + jets background processes, the modelling uncertainties are evaluated using SHERPA samples by varying the renormalization and factorization scales, and the merging and resummation scales. The resulting impact on the total background yields from the Z + jets theoretical uncertainties are up to 19% while the uncertainties due to W + jets variations are less than 5%.

For the $t\bar{t}$ background, uncertainties are evaluated due to the hard scattering generation, the choice of the parton-showering model (comparing POWHEG-BOXPYTHIAvs. HERWIG++ and SHERPA) and the emission of additional partons in the initial and final states [42]. The ISR/FSR modeling of POWHEG-BOXPYTHIA was compared to MG5_AMC@NLO and was found to agree within the total uncertainty. The largest impact of the $t\bar{t}$ theory systematics on the total background yields arises for SRC and is about 11-71%. For the $t\bar{t}+W/Z$ background, the theoretical uncertainty is estimated through variations including the choice of renormalization and factorization scales (each varied up and down by a factor of two), the choice of PDF, as well as a comparison between MC@NLO and OpenLoops+SHERPA generators, resulting in a maximum uncertainty of 6% in SRA-TT. The single-top background is dominated by the Wt subprocess. Uncertainties are evaluated for the choice of the parton-showering model (PYTHIA vs. HERWIG++) and for the emission of additional partons in the initial- and final-state radiation. A 100% uncertainty is
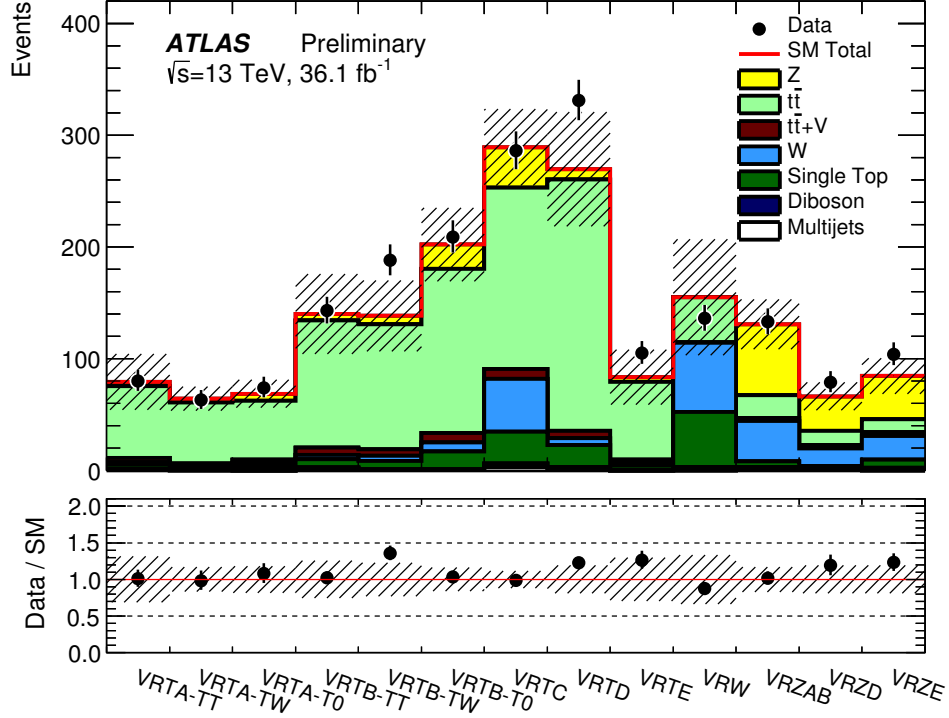
Figure 5: Final yields for all validation regions after the likelihood fit. The stacked histograms show the SM expectation and the hatched uncertainty band around the SM expectation shows total uncertainty which consists of the MC statistical, detector-related systematic uncertainties, and theoretical uncertainties on the extrapolation from CR to VR.

applied to the single top background estimate to account for the effect of interference between single-top quark and $t\bar{t}$ production. The final single top uncertainty relative to the total background estimate is up to 18%. The detector systematics are also applied to the signal samples used for interpretation. Theoretical uncertainties on the signal cross-section as described in Section 4 are treated separately and the limits are given for the $\pm1\sigma$ values as well as the central cross-section. The effect of the ISR/FSR modeling and the scale variations on the acceptance and efficiency are also taken into account when interpreting the results.

9 Results and interpretation

The observed event yields are compared to the total number of expected background events in Tables 9, 10, 11, and Figure 6. The total background estimate is determined from the simultaneous fit based on a procedure described in Section 7. Figure 7 shows the distribution of the E_T^{miss}, $m_{T2}^{\chi^2}$, $m_T^{b,\max}$, m_T, R_{ISR}, and H_T for the various signal regions, with R_{ISR} being shown combining SRC1-5. In these distributions, the background expectations are normalized to the values determined from the simultaneous fit.

Table 9: Observed and expected yields, before and after the fit, for SRA and SRB for an integrated luminosity of $\int \mathcal{L}\, dt$ = 36.1 fb^{-1}. The uncertainties include MC statistical, detector systematic-related uncertainties, and theoretical uncertainties on the extrapolation from CR to SR.

	SRA-TT	SRA-TW	SRA-T0	SRB-TT	SRB-TW	SRB-T0
Observed	11	9	18	38	53	206
Fitted background events						
Total SM	8.6 ± 2.5	9.4 ± 2.9	18.7 ± 5.4	39.4 ± 9.2	52 ± 11	179 ± 40
$t\bar{t}$	0.70 $^{+0.89}_{-0.70}$	0.51 $^{+0.55}_{-0.51}$	1.31 ± 0.71	7.3 ± 4.3	12.4 ± 5.7	43 ± 22
W + jets	0.82 ± 0.17	0.89 ± 0.56	2.00 ± 0.96	7.8 ± 2.9	4.8 ± 1.3	25.8 ± 8.9
Z + jets	2.5 ± 1.6	4.9 ± 2.6	9.8 ± 3.9	9.0 ± 4.2	16.8 ± 6.8	60 ± 20
$t\bar{t}$+W/Z	3.17 ± 0.78	1.85 ± 0.49	2.61 ± 0.64	9.3 ± 2.1	10.8 ± 2.0	20.6 ± 4.2
Single top	1.2 $^{+1.4}_{-1.2}$	0.70 $^{+0.76}_{-0.70}$	2.9 $^{+3.1}_{-2.9}$	4.2 $^{+4.5}_{-4.2}$	5.9 $^{+6.3}_{-5.9}$	26 $^{+28}_{-26}$
Dibosons	––	0.35 ± 0.26	––	0.13 ± 0.07	0.60 ± 0.43	1.04 ± 0.73
Multijets	0.21 ± 0.10	0.14 ± 0.09	0.12 ± 0.07	1.54 ± 0.64	1.01 ± 0.88	1.8 ± 1.5
Expected events before fit						
Total SM	7.1	7.9	16.3	32.4	46.1	162
$t\bar{t}$	0.60	0.45	1.45	6.1	12.8	47
W + jets	0.65	0.70	1.58	6.1	3.83	20.4
Z + jets	2.1	4.2	8.6	7.7	14.4	53
$t\bar{t}$+W/Z	2.46	1.43	2.02	7.3	8.4	15.9
Single top	1.0	0.60	2.5	3.6	5.1	22
Dibosons	––	0.35	––	0.13	0.60	1.03
Multijets	0.21	0.14	0.12	1.54	1.01	1.8

Table 10: Observed and expected yields, before and after the fit, for SRC for an integrated luminosity of $\int \mathcal{L}\, dt = 36.1\,\mathrm{fb}^{-1}$. The uncertainties include MC statistical, detector-related systematic uncertainties, and theoretical uncertainties on the extrapolation from CR to SR.

	SRC1	SRC2	SRC3	SRC4	SRC5
Observed	20	22	22	1	0
Fitted background events					
Total SM	20.6 $\pm$ 6.6	27.5 $\pm$ 4.9	18.9 $\pm$ 3.5	7.7 $\pm$ 1.4	0.90 $\pm$ 0.71
$t\bar{t}$	12.8 $\pm$ 5.9	22.1 $\pm$ 4.2	14.6 $\pm$ 3.2	4.92 $\pm$ 0.98	0.63 $^{+0.69}_{-0.63}$
W + jets	0.81 $\pm$ 0.37	1.93 $\pm$ 0.48	1.91 $\pm$ 0.63	1.93 $\pm$ 0.45	0.21 $\pm$ 0.12
Z + jets	$--$	$--$	$--$	$--$	$--$
$t\bar{t}+W/Z$	0.29 $\pm$ 0.18	0.59 $\pm$ 0.38	0.56 $\pm$ 0.31	0.08 $\pm$ 0.08	0.06 $\pm$ 0.03
Single top	1.7 $^{+2.0}_{-1.7}$	1.2 $^{+1.8}_{-1.2}$	1.2 $^{+1.4}_{-1.2}$	0.72 $^{+0.77}_{-0.72}$	$--$
Dibosons	0.39 $\pm$ 0.33	0.21 $\pm$ 0.11	0.29 $\pm$ 0.18	$--$	$--$
Multijets	4.6 $\pm$ 2.4	1.58 $\pm$ 0.77	0.32 $\pm$ 0.17	0.04 $\pm$ 0.02	$--$
Expected events before fit					
Total SM	25.4	36.0	24.2	9.2	1.11
$t\bar{t}$	18.2	31.2	20.6	7.0	0.89
W + jets	0.64	1.53	1.51	1.53	0.17
Z + jets	$--$	$--$	$--$	$--$	$--$
$t\bar{t}+W/Z$	0.22	0.46	0.44	0.07	0.05
Single top	1.4	1.0	1.0	0.62	$--$
Dibosons	0.39	0.21	0.28	$--$	$--$
Multijets	4.6	1.58	0.32	0.04	$--$

No significant excess above the SM expectation is observed in any of the signal regions. The smallest p-values are 27%, 27%, and 29% for SRB-T0, SRD-high, and SRA-TT, respectively. The 95% confidence level (CL) upper limits on the number of beyond-the-SM (BSM) events in each signal region are derived using the CL$_s$ prescription [72, 73] and calculated from asymptotic formulae [70]. Model-independent limits on the visible BSM cross sections, defined as $\sigma_{\mathrm{vis}} = \sigma \cdot A \cdot \epsilon$, where σ is the production cross section, A is the acceptance, and ϵ is the selection efficiency for a BSM signal, are reported in Table 12.

The detector acceptance multiplied by the efficiency ($A \cdot \epsilon$) is calculated for several signal regions and their benchmark points. The $A \cdot \epsilon$ values for signal regions aimed at high-energy final states, SRA and SRE, is 9% and 6% for their respective signal benchmark points of $m_{\tilde{t}} = 1000$ GeV, $m_{\tilde{\chi}^0} = 1$ GeV, and $m_{\tilde{g}} = 1700$ GeV, $m_{\tilde{t}} = 400$ GeV, $m_{\tilde{\chi}^0} = 395$ GeV. SRB has an $A \cdot \epsilon$ of 1.4% for $m_{\tilde{t}} = 600$ GeV, $m_{\tilde{\chi}^0} = 300$ GeV. For SRD-low and SRD-high, the $A \cdot \epsilon$ (expected number of signal events) is 0.05% (33.4) and 0.5% (10.5) for $m_{\tilde{t}} = 400$ GeV, $m_{\tilde{\chi}^\pm_1} = 100$ GeV, $m_{\tilde{\chi}^0} = 50$ GeV and $m_{\tilde{t}} = 700$ GeV, $m_{\tilde{\chi}^\pm_1} = 200$ GeV, $m_{\tilde{\chi}^0} = 100$ GeV where BF($\tilde{t} \to b\tilde{\chi}^\pm_1$)=100% is assumed, respectively. Finally, SRC1-5 (combining the R_{ISR} windows) has an $A \cdot \epsilon$ of 0.08% for $m_{\tilde{t}} = 400$ GeV, $m_{\tilde{\chi}^0} = 227$ GeV.

Table 11: Observed and expected yields, before and after the fit, for SRD and SRE for an integrated luminosity of $\int \mathcal{L} \, dt = 36.1 \, \text{fb}^{-1}$. The uncertainties include MC statistical, detector-related systematic uncetainties, and theoretical uncertainties on the extrapolation from CR to SR.

	SRD-low	SRD-high	SRE
Observed	27	11	3
Fitted background events			
Total SM	25.2 ± 7.7	8.6 ± 2.4	3.6 ± 1.1
$t\bar{t}$	3.2 ± 3.2	0.98 ± 0.89	$0.21^{+0.39}_{-0.21}$
W + jets	6.1 ± 3.0	1.06 ± 0.34	0.52 ± 0.27
Z + jets	6.9 ± 3.0	3.2 ± 1.3	1.36 ± 0.56
$t\bar{t}+W/Z$	4.0 ± 1.0	1.38 ± 0.39	0.89 ± 0.23
Single top	$3.9^{+4.2}_{-3.9}$	$1.5^{+1.6}_{-1.5}$	$0.66^{+0.70}_{-0.66}$
Dibosons	––	––	––
Multijets	1.12 ± 0.37	0.40 ± 0.15	––
Expected events before fit			
Total SM	22.4	7.7	3.02
$t\bar{t}$	3.4	1.04	0.21
W + jets	4.8	0.84	0.42
Z + jets	6.7	3.1	1.15
$t\bar{t}+W/Z$	3.06	1.07	0.69
Single top	3.3	1.3	0.56
Dibosons	––	––	––
Multijets	1.12	0.40	––

The profile likelihood ratio test statistic is used to set limits on direct pair production of top squarks. The signal strength parameter is allowed to float in the fit [71], and any signal contamination in the CRs is taken into account. Again, limits are derived using the CL_s prescription and calculated from asymptotic formulae. Orthogonal signal subregions, such as SRA-TT, SRA-TW, and SRA-T0, are statistically combined by multiplying their likelihood functions. A similar procedure is performed for the signal subregions in SRB and SRC. Once the signal subregions are combined or chosen, the signal region with the smallest expected 95% CL_s is chosen from SRA, SRB, and SRC for each signal model in the $\tilde{t}$-$\tilde{\chi}_1^0$ signal grid. The nominal event yield in each SR is set to the mean background expectation to determine the expected limits; contours that correspond to $\pm 1\sigma$ uncertainties in the background estimates (σ_{exp}) are also evaluated. The observed event yields determine the observed limits for each SR; these are evaluated for the nominal signal cross sections as well as for $\pm 1\sigma$ theory uncertainties on those cross sections $\sigma_{\text{theory}}^{\text{SUSY}}$.

Figure 8 shows the observed (solid red line) and expected (solid blue line) exclusion limits at 95% CL in the $\tilde{t}$ - $\tilde{\chi}_1^0$ mass plane for $\int \mathcal{L} \, dt = 36.1 \, \text{fb}^{-1}$ for SRA, SRB, and SRC. The data excludes top-squark masses between 450 and 950 GeV for $\tilde{\chi}_1^0$ masses below 160 GeV extending Run 1 limits from the combination of
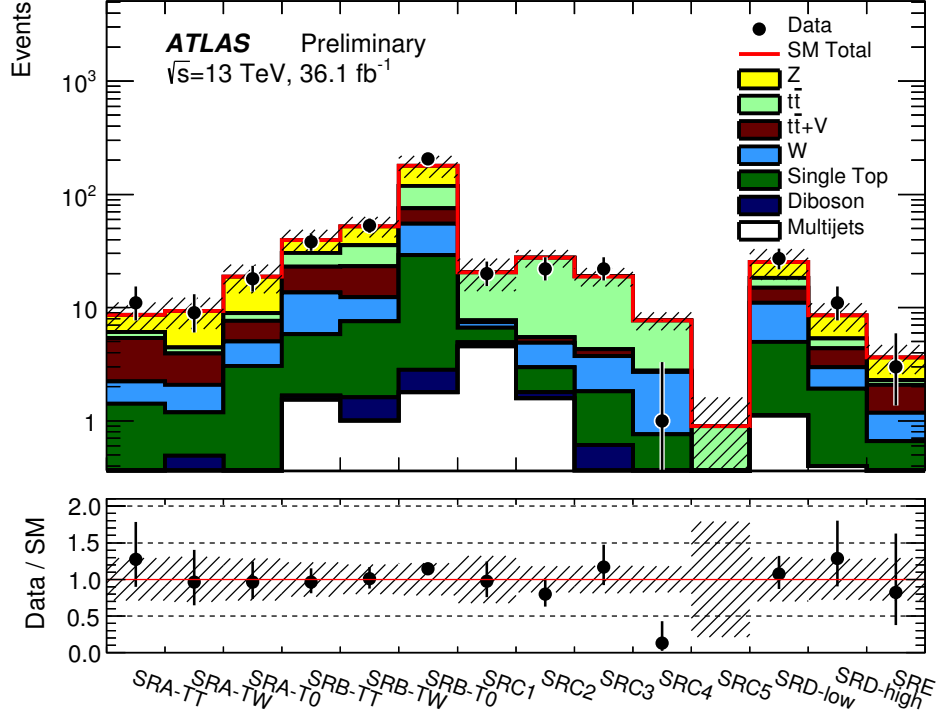
Figure 6: Final yields for all signal regions after the likelihood fit. The stacked histograms show the SM expectation and the hatched uncertainty band around the SM expectation shows total uncertainty which consists of the MC statistical, detector-related systematic uncertainties, and theoretical uncertainties on the extrapolation from CR to SR.

zero- and one-lepton channels by 250 GeV. Additional constraints are set in the case when $m_{\tilde{t}} \approx m_t + m_{\tilde{\chi}^0}$, for which top-squark masses between $235-590$ GeV are excluded. The limits in this region of the exclusion are new compared to the 8 TeV results and come from the inclusion of SRC which takes advantage of an ISR system to discriminate between signal and the dominant $t\bar{t}$ background.

The SRE results are interpreted for indirect top-squark production through gluino decays in terms of the $\tilde{\chi}^0_1$ vs. $\tilde{g}$ mass plane with $\Delta m(\tilde{t}, \tilde{\chi}^0_1) = 5$ GeV. Gluino masses up to $m_{\tilde{g}} = 1800$ GeV with $m_{\tilde{\chi}^0} < 800$ GeV are excluded are shown in Fig. 9.

Figure 7: Distributions of E_T^{miss} for SRA-TT, $m_{T2}^{\chi^2}$ for SRA-T0, $m_T^{b,max}$ for SRB-TW, R_{ISR} for SRC1-5, $m_T^{b,max}$ for SRD-high and H_T for SRE after the likelihood fit. The stacked histograms show the SM expectation and the hatched uncertainty band around the SM expectation shows the MC statistical and detector-related systematic uncertainties. A representative signal point is shown for each distribution.

Table 12: Left to right: 95% CL upper limits on the visible cross section ($\langle\sigma A\epsilon\rangle^{95}_{\text{obs}}$) and on the number of signal events (S^{95}_{obs}). The third column (S^{95}_{exp}) shows the 95% CL upper limit on the number of signal events, given the expected number (and $\pm 1\sigma$ excursions on the expectation) of background events. The two columns before last indicate the CL_B value, i.e. the confidence level observed for the background-only hypothesis, and the discovery p-value ($p(s = 0)$) and the significance (σ).

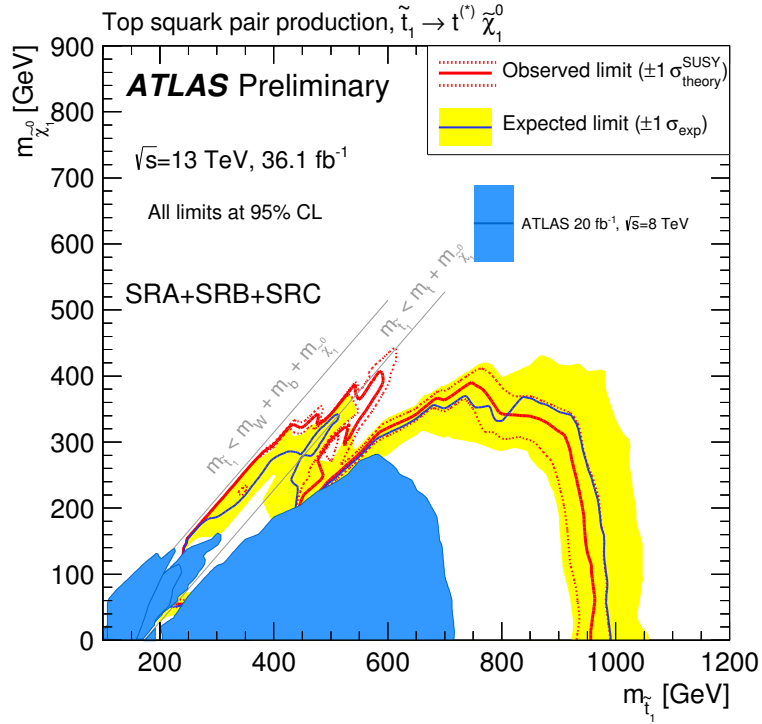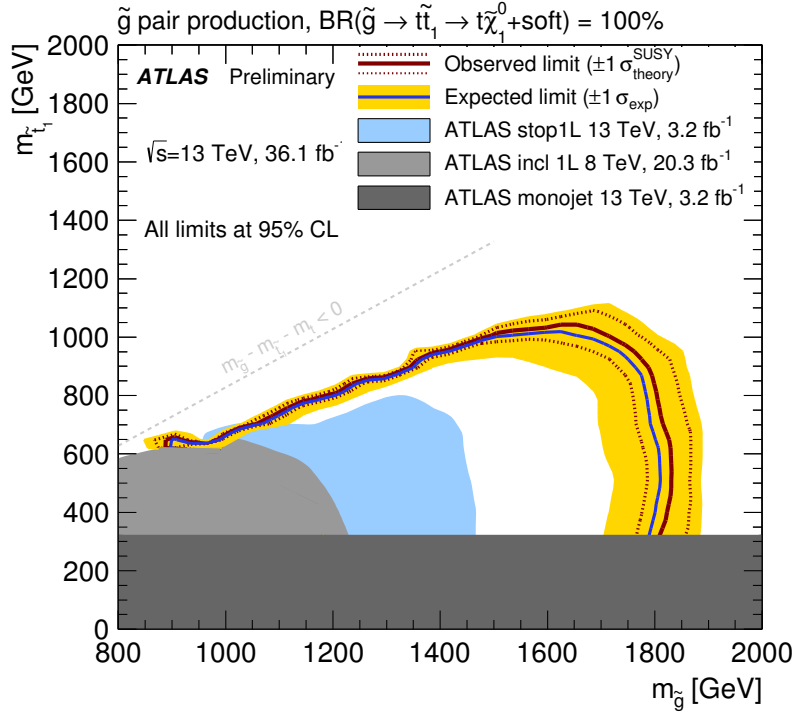| Signal channel	$\langle\sigma A\epsilon\rangle^{95}_{\text{obs}}$[fb]	S^{95}_{obs}	S^{95}_{exp}	CL_B	$p(s = 0)$ (Z)
SRA-TT	0.31	11.2	$9.1^{+4.3}_{-2.5}$	0.69	0.29 (0.57)
SRA-TW	0.25	9.0	$9.2^{+3.6}_{-2.8}$	0.47	0.50 (0.00)
SRA-T0	0.40	14.6	$14.9^{+5.2}_{-4.3}$	0.46	0.50 (0.00)
SRB-TT	0.65	23.4	$24.0^{+7.8}_{-6.8}$	0.46	0.50 (0.00)
SRB-TW	0.73	26.2	$26.0^{+8.8}_{-6.6}$	0.52	0.48 (0.05)
SRB-T0	2.93	106	91^{+24}_{-22}	0.72	0.27 (0.61)
SRC1	0.44	16.0	$16.3^{+5.8}_{-4.2}$	0.47	0.50 (0.00)
SRC2	0.35	12.6	$15.5^{+5.9}_{-4.2}$	0.26	0.50 (0.00)
SRC3	0.44	15.8	$12.8^{+4.7}_{-2.7}$	0.69	0.30 (0.54)
SRC4	0.09	3.1	$6.5^{+3.3}_{-2.1}$	0.02	0.50 (0.00)
SRC5	0.06	3.0	$3.9^{+1.0}_{-0.3}$	0.32	0.50 (0.00)
SRD-low	0.57	20.7	$19.8^{+6.8}_{-4.9}$	0.57	0.43 (0.19)
SRD-high	0.32	11.6	$9.6^{+3.9}_{-2.4}$	0.71	0.27 (0.60)
SRE	0.14	5.0	$5.6^{+2.7}_{-1.7}$	0.40	0.50 (0.00)

Figure 8: Expected (blue solid line) and observed (red solid line) exclusion limits at 95% CL as a function of $\tilde{t}$ and $\tilde{\chi}_1^0$ masses in the scenario where both top squarks decay via $\tilde{t} \to t^{(*)} \tilde{\chi}_1^0$. Uncertainty bands corresponding to the $\pm 1\sigma$ variation on the expected limit (yellow band) and the sensitivity of the observed limit to $\pm 1\sigma$ variations of the signal theoretical uncertainties (red dotted lines) are also indicated. Observed limits from all third-generation Run 1 searches [74] at $\sqrt{s} = 8$ TeV centre-of-mass energy are overlaid for comparison in blue.

Figure 9: Expected (blue solid line) and observed (red solid line) exclusion limits at 95% CL exclusion as a function of $\tilde{g}$ and $\tilde{t}$ masses in the scenario where both gluinos decay via $\tilde{g} \rightarrow t\tilde{t} \rightarrow t\tilde{\chi}_1^0$+soft and $\Delta m(\tilde{t}, \tilde{\chi}_1^0) = 5$ GeV. Uncertainty bands corresponding to the $\pm 1\sigma$ variation on the expected limit (yellow band) and the sensitivity of the observed limit to $\pm 1\sigma$ variations of the signal theoretical uncertainties (red dotted lines) are also indicated. Observed limits from previous searches with the ATLAS detector at $\sqrt{s} = 8$ and $\sqrt{s} = 13$ TeV are overlaid in grey and blue [75–77].

10 Conclusions

Results from a search for top squark production based on integrated luminosity of $\int \mathcal{L}\, dt = (36.1 \pm 1.2)$ fb^{-1} data of $\sqrt{s} = 13$ TeV pp collisions recorded by the ATLAS experiment at the LHC in 2015 and 2016 are presented. Top squarks are searched for in final states with high-p_T jets and large missing transverse momentum. In this note, the top squark is assumed to decay via $\tilde{t} \to t^{(*)} \tilde{\chi}_1^0$ with large or small mass differences between the top squark and the neutralino $\Delta m(\tilde{t}, \tilde{\chi}_1^0)$. Gluino-mediated $\tilde{t}$ production is studied in which gluinos decay via $\tilde{g} \to t\tilde{t}$, with a small $\Delta m(\tilde{t}, \tilde{\chi}_1^0)$.

No significant excess above the expected SM background prediction is observed. Exclusion limits at 95% confidence level on the combination of top squark and LSP mass are derived resulting in the exclusion of top squark masses in the range 450−950 GeV for $\tilde{\chi}_1^0$ masses below 160 GeV. For the case where $m_{\tilde{t}} \sim m_t + m_{\tilde{\chi}^0}$, top squark masses between 235−590 GeV are excluded. Finally, exclusion limits are produced for gluino production resulting in gluino masses being constraint to be above 1800 GeV for $\tilde{\chi}_1^0$ masses below 800 GeV.

References

[1] Yu. A. Golfand and E. P. Likhtman,
Extension of the Algebra of Poincare Group Generators and Violation of p Invariance,
JETP Lett. **13** (1971) 323, [Pisma Zh. Eksp. Teor. Fiz.13,452(1971)].

[2] D. V. Volkov and V. P. Akulov, *Is the Neutrino a Goldstone Particle?*, Phys. Lett. B **46** (1973) 109.

[3] J. Wess and B. Zumino, *Supergauge Transformations in Four-Dimensions*,
Nucl. Phys. B **70** (1974) 39.

[4] J. Wess and B. Zumino, *Supergauge Invariant Extension of Quantum Electrodynamics*,
Nucl. Phys. B **78** (1974) 1.

[5] S. Ferrara and B. Zumino, *Supergauge Invariant Yang-Mills Theories*,
Nucl. Phys. B **79** (1974) 413.

[6] A. Salam and J. A. Strathdee, *Supersymmetry and Nonabelian Gauges*,
Phys. Lett. B **51** (1974) 353.

[7] S. Dimopoulos and H. Georgi, *Softly Broken Supersymmetry and SU(5)*,
Nucl. Phys. B **193** (1981) 150.

[8] N. Sakai, *Naturalness in Supersymmetric Guts*, Z. Phys. C **11** (1981) 153.

[9] S. Dimopoulos, S. Raby and F. Wilczek, *Supersymmetry and the scale of unification*,
Phys. Rev. D **24** (6 1981) 1681,
URL: http://link.aps.org/doi/10.1103/PhysRevD.24.1681.

[10] L. Ibáñez and G. Ross, *Low-energy predictions in supersymmetric grand unified theories*,
Physics Letters B **105** (1981) 439 , ISSN: 0370-2693,
URL: http://www.sciencedirect.com/science/article/pii/0370269381912004.

[11] G. R. Farrar and P. Fayet, *Phenomenology of the Production, Decay, and Detection of New Hadronic States Associated with Supersymmetry*, Phys. Lett. B **76** (1978) 575.

[12] W. Beenakker et al., *Stop production at hadron colliders*, Nucl. Phys. **B 515** (1998) 3.

[13] W. Beenakker et al., *Supersymmetric top and bottom squark production at hadron colliders*, JHEP **08** (2010) 098, arXiv: 1006.4771 [hep-ph].

[14] W. Beenakker et al., *Squark and gluino hadroproduction*, Int. J. Mod. Phys. **A 26** (2011) 2637.

[15] C. Borschensky et al., *Squark and gluino production cross sections in pp collisions at $\sqrt{s}$ = 13, 14, 33 and 100 TeV*, Eur. Phys. J. C **74** (2014) 3174, arXiv: 1407.5066 [hep-ph].

[16] H. Goldberg, *Constraint on the Photino Mass from Cosmology*, Phys. Rev. Lett. **50** (1983) 1419, [Erratum: Phys. Rev. Lett.103,099905(2009)].

[17] J. R. Ellis et al., *Supersymmetric Relics from the Big Bang*, Nucl. Phys. B **238** (1984) 453.

[18] ATLAS Collaboration, *Search for direct pair production of the top squark in all-hadronic final states in proton-proton collisions at $\sqrt{s}$ = 8 TeV with the ATLAS detector*, JHEP **09** (2014) 015, arXiv: 1406.1122 [hep-ex].

[19] ATLAS Collaboration, *ATLAS Run 1 searches for direct pair production of third-generation squarks at the Large Hadron Collider*, Eur. Phys. J. **C75** (2015) 510, [Erratum: Eur. Phys. J.C76,no.3,153(2016)], arXiv: 1506.08616 [hep-ex].

[20] CMS Collaboration, *Search for Supersymmetry Using Razor Variables in Events with b-Tagged Jets in pp Collisions at $\sqrt{s}$ = 8 TeV*, Phys. Rev. **D91** (2015) 052018, arXiv: 1502.00300 [hep-ex].

[21] CMS Collaboration, *Searches for Supersymmetry using the M_{T2} Variable in Hadronic Events Produced in pp Collisions at 8 TeV*, JHEP **05** (2015) 078, arXiv: 1502.04358 [hep-ex].

[22] CMS Collaboration, *Search for top squark pair production in compressed-mass-spectrum scenarios in proton-proton collisions at $\sqrt{s}$ = 8 TeV using the alpha[T] variable*, Phys. Lett. **B767** (2017) 403, arXiv: 1605.08993 [hep-ex].

[23] CMS Collaboration, *Searches for pair production for third-generation squarks in sqrt(s)=13 TeV pp collisions*, (2016), arXiv: 1612.03877 [hep-ex].

[24] CMS Collaboration, *Search for supersymmetry in the all-hadronic final state using top quark tagging in pp collisions at $\sqrt{s}$ = 13 TeV*, (2017), arXiv: 1701.01954 [hep-ex].

[25] ATLAS Collaboration, *The ATLAS Experiment at the CERN Large Hadron Collider*, JINST **3** (2008) S08003.

[26] ATLAS Collaboration, *ATLAS Insertable B-Layer Technical Design Report*, (2010), URL: https://cds.cern.ch/record/1291633.

[27] ATLAS Collaboration, *Performance of the ATLAS Trigger System in 2015*, (2016), arXiv: 1611.09661 [hep-ex].

[28] ATLAS Collaboration, *Luminosity determination in pp collisions at $\sqrt{s}$ = 8 TeV using the ATLAS detector at the LHC*, Eur. Phys. J. **C76** (2016) 653, arXiv: 1608.03953 [hep-ex].

[29] J. Alwall et al., *The automated computation of tree-level and next-to-leading order differential cross sections, and their matching to parton shower simulations*, JHEP **07** (2014) 079, arXiv: 1405.0301 [hep-ph].

[30] T. Sjostrand, S. Mrenna and P. Z. Skands, *A Brief Introduction to PYTHIA 8.1*, Comput. Phys. Commun. **178** (2008) 852, arXiv: `0710.3820 [hep-ph]`.

[31] D. J. Lange, *The EvtGen particle decay simulation package*, Nucl. Instrum. Meth. **462** (2001) 152 , BEAUTY2000, Proceedings of the 7th Int. Conf. on B-Physics at Hadron Machines, ISSN: 0168-9002, URL: `http://www.sciencedirect.com/science/article/pii/S0168900201000894`.

[32] R. D. Ball et al., *Parton distributions with LHC data*, Nucl. Phys. B **867** (2013) 244, arXiv: `1207.1303 [hep-ph]`.

[33] ATLAS Collaboration, *ATLAS Run 1 Pythia8 tunes*, ATL-PHYS-PUB-2014-021, 2014, URL: `https://cds.cern.ch/record/1966419`.

[34] L. Lönnblad and S. Prestel, *Merging Multi-leg NLO Matrix Elements with Parton Showers*, JHEP **03** (2013) 166, arXiv: `1211.7278 [hep-ph]`.

[35] T. Gleisberg et al., *Event generation with SHERPA 1.1*, JHEP **02** (2009) 007, arXiv: `0811.4622 [hep-ph]`.

[36] S. Alioli et al., *A general framework for implementing NLO calculations in shower Monte Carlo programs: the POWHEG BOX*, JHEP **06** (2010) 043, arXiv: `1002.2581 [hep-ph]`.

[37] T. Sjöstrand, S. Mrenna and P. Skands, *PYTHIA 6.4 Physics and Manual*, JHEP **05** (2006) 026, arXiv: `hep-ph/0603175`.

[38] H.-L. Lai et al., *New parton distributions for collider physics*, Phys. Rev. **D82** (2010) 074024, arXiv: `1007.2241 [hep-ph]`.

[39] P. Z. Skands, *Tuning Monte Carlo Generators: The Perugia Tunes*, Phys. Rev. **D82** (2010) 074018, arXiv: `1005.3457 [hep-ph]`.

[40] ATLAS Collaboration, *Monte Carlo Generators for the Production of a W or Z/γ^* Boson in Association with Jets at ATLAS in Run 2*, ATL-PHYS-PUB-2016-003, 2016, URL: `https://cds.cern.ch/record/2120133`.

[41] ATLAS Collaboration, *Multi-Boson Simulation for 13 TeV ATLAS Analyses*, ATL-PHYS-PUB-2016-002, 2016, URL: `https://cds.cern.ch/record/2119986`.

[42] ATLAS Collaboration, *Simulation of top quark production for the ATLAS experiment at sqrt(s) = 13 TeV*, ATL-PHYS-PUB-2016-004, 2016, URL: `https://cds.cern.ch/record/2120417`.

[43] ATLAS Collaboration, *Modelling of the $t\bar{t}H$ and $t\bar{t}V$ ($V = W, Z$) processes for $\sqrt{s}$ = 13 TeV ATLAS analyses*, ATL-PHYS-PUB-2016-005, 2016, URL: `https://cds.cern.ch/record/2120826`.

[44] ATLAS Collaboration, *Validation of Monte Carlo event generators in the ATLAS Collaboration for LHC Run 2*, ATL-PHYS-PUB-2016-001, 2016, URL: `https://cds.cern.ch/record/2119984`.

[45] ATLAS Collaboration, *The ATLAS Simulation Infrastructure*, Eur. Phys. J. **C70** (2010) 823, arXiv: `1005.4568 [physics.ins-det]`.

[46] S. Agostinelli et al., *GEANT4: A Simulation toolkit*, Nucl. Instrum. Meth. **A506** (2003) 250.

[47] ATLAS Collaboration, *The simulation principle and performance of the ATLAS fast calorimeter simulation FastCaloSim*, ATL-PHYS-PUB-2010-013, 2010, URL: `https://cds.cern.ch/record/1300517`.

[48] ATLAS Collaboration, *Summary of ATLAS Pythia 8 tunes*, ATL-PHYS-PUB-2012-003, 2012, URL: https://cds.cern.ch/record/1474107.

[49] A. D. Martin et al., *Parton distributions for the LHC*, Eur. Phys. J. **C63** (2009) 189, arXiv: 0901.0002 [hep-ph].

[50] ATLAS Collaboration,
Vertex Reconstruction Performance of the ATLAS Detector at $\sqrt{s}$ = 13 TeV,
ATL-PHYS-PUB-2015-026, 2015, URL: https://cds.cern.ch/record/2037717.

[51] ATLAS Collaboration, *Calorimeter Clustering Algorithms: Description and Performance*,
ATL-LARG-PUB-2008-002, 2008, URL: https://cds.cern.ch/record/1099735.

[52] M. Cacciari, G. P. Salam and G. Soyez, *The Anti-k(t) jet clustering algorithm*,
JHEP **04** (2008) 063, arXiv: 0802.1189 [hep-ph].

[53] M. Cacciari, G. P. Salam and G. Soyez, *FastJet User Manual*, Eur. Phys. J. C **72** (2012) 1896,
arXiv: 1111.6097 [hep-ph].

[54] M. Cacciari and G. P. Salam, *Pileup subtraction using jet areas*, Phys. Lett. **B659** (2008) 119,
arXiv: 0707.1378 [hep-ph].

[55] ATLAS Collaboration, *Jet Calibration and Systematic Uncertainties for Jets Reconstructed in the ATLAS Detector at $\sqrt{s}$ = 13 TeV*, ATL-PHYS-PUB-2015-015, 2015,
URL: https://cds.cern.ch/record/2037613.

[56] ATLAS Collaboration,
Selection of jets produced in 13TeV proton-proton collisions with the ATLAS detector,
ATLAS-CONF-2015-029, 2015, URL: https://cds.cern.ch/record/2037702.

[57] ATLAS Collaboration, *Tagging and suppression of pileup jets with the ATLAS detector*,
ATLAS-CONF-2014-018, 2014, URL: https://cds.cern.ch/record/1700870.

[58] ATLAS Collaboration,
Commissioning of the ATLAS b-tagging algorithms using $t\bar{t}$ events in early Run-2 data,
ATL-PHYS-PUB-2015-039, 2015, URL: https://cds.cern.ch/record/2047871.

[59] ATLAS Collaboration, *Optimisation of the ATLAS b-tagging performance for the 2016 LHC Run*,
ATL-PHYS-PUB-2016-012, 2016, URL: https://cds.cern.ch/record/2160731.

[60] ATLAS Collaboration, *b-tagging in dense environments*, ATL-PHYS-PUB-2014-014, 2014,
URL: https://cds.cern.ch/record/1750682.

[61] ATLAS Collaboration, *Electron efficiency measurements with the ATLAS detector using 2012 LHC proton-proton collision data*, (2016), arXiv: 1612.01456 [hep-ex].

[62] ATLAS Collaboration, *Performance of algorithms that reconstruct missing transverse momentum in $\sqrt{s}$ = 8 TeV proton-proton collisions in the ATLAS detector*, (2016),
arXiv: 1609.09324 [hep-ex].

[63] ATLAS Collaboration, *Muon reconstruction performance of the ATLAS detector in proton–proton collision data at $\sqrt{s}$ =13 TeV*, Eur. Phys. J. **C76** (2016) 292, arXiv: 1603.05598 [hep-ex].

[64] C. Lester and D. Summers,
Measuring masses of semiinvisibly decaying particles pair produced at hadron colliders,
Phys. Lett. **B463** (1999) 99, arXiv: hep-ph/9906349.

[65] A. Barr, C. Lester and P. Stephens, *m(T2): The Truth behind the glamour*,
J. Phys. **G29** (2003) 2343, arXiv: hep-ph/0304226 [hep-ph].

[66] H. An and L.-T. Wang, *Opening up the compressed region of top squark searches at 13 TeV LHC*,
Phys. Rev. Lett. **115** (2015) 181602, arXiv: 1506.00653 [hep-ph].

[67] S. Macaluso et al., *Revealing Compressed Stops Using High-Momentum Recoils*,
JHEP **03** (2016) 151, arXiv: 1506.07885 [hep-ph].

[68] P. Jackson, C. Rogan and M. Santoni, *Sparticles in motion: Analyzing compressed SUSY scenarios with a new method of event reconstruction*, Phys. Rev. **D95** (2017) 035031,
arXiv: 1607.08307 [hep-ph].

[69] ATLAS Collaboration, *Search for squarks and gluinos with the ATLAS detector in final states with jets and missing transverse momentum using 4.7 fb^{-1} of $\sqrt{s}$ = 7 TeV proton-proton collision data*,
Phys. Rev. **D87** (2013) 012008, arXiv: 1208.0949 [hep-ex].

[70] G. Cowan et al., *Asymptotic formulae for likelihood-based tests of new physics*,
Eur. Phys. J. **C71** (2011) 1554, [Erratum: Eur. Phys. J.C73,2501(2013)],
arXiv: 1007.1727 [physics.data-an].

[71] M. Baak et al., *HistFitter software framework for statistical data analysis*,
Eur. Phys. J. **C75** (2015) 153, arXiv: 1410.1280 [hep-ex].

[72] T. Junk, *Confidence level computation for combining searches with small statistics*,
Nucl. Instrum. Meth. **A434** (1999) 435, arXiv: hep-ex/9902006 [hep-ex].

[73] A. L. Read, *Presentation of search results: The CL(s) technique*, J. Phys. **G 28** (2002) 2693.

[74] ATLAS Collaboration, *ATLAS Run 1 searches for direct pair production of third-generation squarks at the Large Hadron Collider*,
Eur. Phys. J. **C75** (2015) 510, [Erratum: Eur. Phys. J.C76,no.3,153(2016)],
arXiv: 1506.08616 [hep-ex].

[75] ATLAS Collaboration, *Search for top squarks in final states with one isolated lepton, jets, and missing transverse momentum in $\sqrt{s}$ = 13 TeV pp collisions with the ATLAS detector*,
Phys. Rev. **D94** (2016) 052009, arXiv: 1606.03903 [hep-ex].

[76] ATLAS Collaboration, *Search for squarks and gluinos in events with isolated leptons, jets and missing transverse momentum at $\sqrt{s}$ = 8 TeV with the ATLAS detector*, JHEP **04** (2015) 116,
arXiv: 1501.03555 [hep-ex].

[77] ATLAS Collaboration, *Search for new phenomena in final states with an energetic jet and large missing transverse momentum in pp collisions at $\sqrt{s}$ = 13 TeV using the ATLAS detector*,
Phys. Rev. **D94** (2016) 032005, arXiv: 1604.07773 [hep-ex].